ЖУРНАЛ СТРУКТУРНОЙ ХИМИИ

2017. Том 58, № 8 *Ноябрь – декабрь* *С. 1661 – 1674*

UDC 548.737:546

REACTION MECHANISM OF THE PREFERENTIAL OXIDATION OF THE CO REACTION IN AN H_2 STREAM OVER Cu—Ni BIMETALLIC CATALYSTS: A COMPUTATIONAL STUDY

N. Liu, L. Guo, C. Wen, Z. Cao

School of Chemistry and Materials Science, Shanxi Normal University, Linfen, P. R. China
E-mail: gl-guoling@163.com

Received December, 25, 2015

The preferential oxidation (PROX, $CO + H_2 + O_2 \rightarrow CO_2 + H_2O$) of the CO reaction in an H_2 stream is the simplest and most cost-effective method to remove CO gas to less than 10 ppm in reformed fuel gas. We study the mechanism of PROX of the CO reaction in the H_2 stream catalyzed by Cu_nNi (n = 3—12) clusters using a density functional theory (DFT) calculation to investigate bimetallic effects on the catalytic activation. Our results indicate that the $Cu_{12}Ni$ cluster is the most efficient catalyst for H_2 dissociation and the Cu_6Ni cluster is the most efficient catalyst for CO-PROX in excess hydrogen among Cu_nNi (n = 3—12) clusters. To gain insight into the adsorption and dissociation of the H_2 molecule effect in the catalytic activity over the $Cu_{12}Ni$ cluster and the potential energy surfaces about PROX of CO oxidation on the Cu_6Ni cluster, the nature of the interaction between the adsorbate and substrate is analyzed by detailed electron local densities of states (LDOS) as well as molecular structures.

DOI: 10.26902/JSC20170819

K e y w o r d s: CO-PROX in the H_2 stream, mechanism, Cu_nNi (n = 3—12) clusters catalyzed, density functional theory.

INTRODUCTION

Proton-exchange membrane fuel cells (PEMFC) have attracted much attention in the application to electric vehicles or residential power-generations because of many fascinating features such as a high power density, a rapid start-up, and a high efficiency [1]. However, at present, the production and delivery of pure hydrogen to the PEMFC anode remain one of the most important relevant scientific challenges, since the poisoning of a Pt-based anode by CO in hydrogen is an awkward problem. To avoid it, the CO concentration in reformed fuel gas must be less than 10 ppm in H_2 [2, 3]. For this purpose, the preferential oxidation (PROX) of the CO reaction appears to be the simplest and most cost-effective method [4] to remove CO gas.

The first patent for the PROX catalyst was awarded to Engelhard in the 1960′s [5], in which supported Pt catalysts were applied to purify hydrogen for the application in the ammonia synthesis. Later on, various catalyst formulations have been developed, among which noble metal catalysts have received much attention for their significantly improved catalytic activities in the low-temperature range [6—8]. P. Sangeetha et al. have studied that Au/TiO_2 catalysts remove CO below 10 ppm in H_2 at 80—180 °C poorly by the deposition-precipitation method due to H_2 competing with CO at high temperatures [9]. A. Fukuoka et al. [10] have found that Pt nanoparticles in mesoporous silica give the unprecedented activity, selectivity, and durability in the PROX reaction below 353 K.

Moreover, the structure of bimetallic nanoparticles has a great impact on catalytic performance. Their higher flexibility in the chemical composition and interatomic arrangement compared to pure metals can open a new reaction pathway, and hence, improve both reactivity and selectivity of catalysts. H. Zhang [11] has shown that Pd—Pt nanocages exhibit both enhanced activity and selectivity for CO oxidation in excess hydrogen than those of Pd nanocubes. E.-Y. Ko [12] and their co-workers have reported that the Pt—Co bimetallic catalyst is more active than monometallic Pt or a core-shell structure supported on yttria-stabilized zirconia (YSZ) for PROX in a H_2-rich gas stream, but Pt—Co was mostly in the CoO form.

The high cost of precious metals has encouraged researchers around the world to look for alternative catalysts. Copper (Cu) is a common and cheap metal with better malleability. Cu-based metals have been demonstrated to possess good catalytic activities for molecules, such as CO, H_2, H_2S, and NO [13—16], and are applied in different areas [17]. Among them, Cu-based metals have especially attracted much attention for PROX applications [18, 19]. Alloyed Pt—Cu has been found to have a much higher activity for the PROX reaction than Pt [20, 21]. These reports have shown that the catalytic performance is strongly dependent on the structure of bimetallic species. L.-Y. Gan *et al*. [22] have deduced that the selectivity of Cu—Ni bimetallic catalysts toward WGS would decrease with increasing Ni concentration. Nevertheless, to our knowledge, for Cu—Ni bimetallic systems, we are unaware of many systematic experimental and theoretical studies on PROX of the CO reaction.

Therefore, we explore the possibility of CO-PROX on Cu_nNi (n = 3—12) alloy clusters at the theoretical level predicting the nature of their active sites. Computational methods became an important tool in providing data on atomic and molecular clusters that give a valuable insight into the mechanisms of the molecule surface binding and the structures of adsorption complexes.

In this work, we investigate the structure of Cu_nNi (n = 3—12) clusters, H_2 adsorption and dissociation, and the detailed reaction mechanisms of CO-PROX catalyzed by Cu_nNi (n = 3—12) clusters from the first-principles theory. Our results indicate that $Cu_{12}Ni$ is the most efficient catalyst for the H_2 dissociation and the Cu_6Ni cluster is the most efficient catalyst for CO-PROX in excess hydrogen among Cu_nNi (n = 3—12) clusters. We hope the understanding of CO-PROX on Cu_nNi (n = 3—12) clusters could give a useful insight into CO-PROX with other catalyzed alloy clusters.

COMPUTATIONAL DETAILS

All of the calculations are carried out with the Gaussian09 program [23]. Full optimized structures and normal-mode frequencies are found using the Perdew-Burke-Ernzerhof (PBE) functional [24]. The standard 6-31G* basis set, which includes polarization functions, was used for hydrogen, oxygen and carbon. The LANL2DZ pseudopotential is adopted for the valence electrons of copper and nickel, and their core electrons are represented by the LANL2DZ effective core potential (ECP) [25, 26]. This scheme is a good compromise between accuracy and computational effort. No symmetric constraints were imposed during geometrical optimizations. Energy and geometry optimizations of the adsorbed species were performed by taking into account various adsorption sites on the catalyst and different binding configurations of the adsorbates. The natural bond orbital (NBO) analysis [27] was used to determine the charge transfer associated with O_2 adsorption. The quadratic synchronous transit (QST) method [28] was used in determining the transition state (TS) geometries. The nature (minima or first-order saddle points) of the optimized structures is identified by the subsequent frequency calculations that also provide zero-point energy (ZEP) corrections. Intrinsic reaction coordinate (IRC) [29] calculations have been performed to verify that each saddle point links two desired minima.

In this work, we calculated the zero-point energy (ZPE) corrected binding energy (BE) of adsorbate A with an Cu_nNi (n = 3—12) cluster defined as

$$BE = (E_{\text{tot}} - E_{\text{Cu}_n\text{Ni}} - E_{\text{A}}) + \left(E_{\text{tot}}^{ZPE} - E_{\text{Cu}_n\text{Ni}}^{ZPE} - E_{\text{A}}^{ZPE}\right).$$

Furthermore, the adsorption energies (E_{ad}) of O_2 with Cu_nNiH_2 (n = 3—12) were calculated as

$$E_{\text{ad}} = (E_{\text{tot}} - E_{\text{Cu}_n\text{NiH}_2} - E_{\text{O}_2}) + \left(E_{\text{tot}}^{ZPE} - E_{\text{Cu}_n\text{NiH}_2}^{ZPE} - E_{\text{O}_2}^{ZPE}\right).$$

Table 1

Comparison of our calculated results and experimental data for Ni_2, Cu_2, *and* CuNi, *d is the bond length in* Å, E_b *is binding energies, and* VIP *is vertical ionization potentials. All energies are in* eV

Systems	Parameters	This work	Experimental
Ni_2	$d_{Ni—Ni}$	2.14	2.155[b]
	E_b	2.63	2.36±0.22[a]
	VIP_{Ni2}	8.06	
Cu_2	$d_{Cu—Cu}$	2.24	2.22[b]
	E_b	2.30	2.01±0.08[a]
	VIP_{Cu2}	7.94	7.894±0.015[a]
CuNi	$d_{Cu—Ni}$	2.24	2.235[b]
	E_b	2.30	2.10[b]
	VIP_{CuNi}	7.63	

[a] Ref. [31].
[b] Ref. [32].

In the aforementioned equations, E_{tot}, E_{Cu_nNi}, E_A, E_{O_2} correspond to the energies of adsorbed species on the Cu_nNi clusters, bare Cu_nNi clusters, and a gas-phase adsorbate, respectively. More negative *BE* and E_{ad} correspond to stronger adsorption.

In order to test the reliability of our calculation, O_2, CO, CO_2, Cu_2, Ni_2 and CuNi are calculated. The calculated bond lengths of O_2, CO and CO_2 at the PBE/6-31G* level are 1.23, 1.15, 1.18 Å, and their binding energy values are 6.24, 11.47, and 17.73 eV, respectively. The corresponding experimental values [30] are 1.21, 1.14, 1.16 Å and 5.23, 11.23, 17.08 eV. This shows the reliability of the basis set and the functional used in our calculations. The accuracy and reliability of the chosen functional and ECP for describing Cu—Ni bimetallic clusters have been confirmed by the calculation of Cu_2, Ni_2 and CuNi. The results are summarized in Table 1; our results are in good agreement with the previous experimental and theoretical data.

RESULTS AND DISCUSSION

Structures of Cu_nNi (n = 3—12) clusters. In cluster physics, one of the most fundamental problems is to determine the ground state geometry. The selection of distinct initial geometries is important for the reliability of the ground state structures obtained. As the cluster size increases, the number of the possible geometries increases dramatically. In this paper, the conformations of pure Cu_n (n = 4—13) clusters are obtained by reference [33, 34]. In the course of choosing initial structures of the Cu_nNi clusters, we have considered possible isomeric structures by placing the Ni atom on each possible site of the Cu_n cluster as well as by substituting one Ni atom by a Cu atom from the Cu_{n+1} cluster. For all isomers of each cluster, the local minima of the potential energy surface are guaranteed by the harmonic vibrational frequencies without imaginary modes. Further, different spin multiplicities of the low-lying energy isomers are considered. When the total energy decreases with increasing spin multiplicity, we consider an increasingly higher spin state until the energy minimum with respect to spin multiplicity is reached.

Correspondingly, at first we studied the ground state structures of Cu_nNi clusters, which are shown in Fig. 1, ***n*a** (n = 6, 12) and Fig. S1, ***n*a** (n = 3, 4, 5, 7, 8, 9, 10, and 11). The electronic states and symmetries of the clusters are consigned in parenthesis in Fig. 1. For Cu_3Ni, the most energetically favorable configuration is a planar rhombus with C_{2v} symmetry (Fig. S1, **3a**), which can be described as the replacement of the Cu atom located at a short diagonal position by one Ni atom in the rhombus Cu_4 [33] structure, rendering the three-coordinated Ni atom. The theoretical Cu—Ni bond

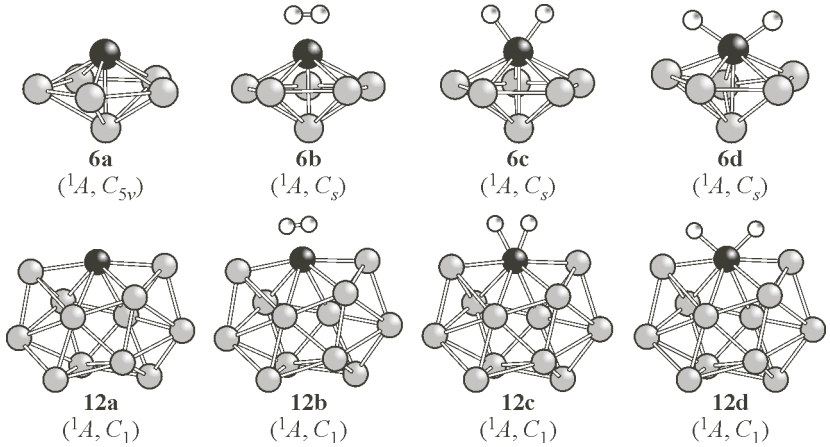

Fig. 1. The lowest-energy structures of Cu_nNi (**na**), $Cu_nNi—H_2$ (**nb**), and Cu_nNiH_2 (**nc**) (for brevity, $n = 6$ and 12).
Dark grey, black, and white balls are used for Cu, Ni, and H respectively. The electronic states and symmetries of the complex are consigned in parenthesis

length is 2.394 Å. E. Florez *et al.* [35] reported a theoretical bond length of 2.42 Å for the Cu—Ni bond, using DFT. The spin triplet Cu_4Ni with the C_{2v} symmetry is a trapezoid-like structure (Fig. S1, **4a**) in which a Ni atom occupies the central position of Cu_5 [33]. For spin doublet Cu_5Ni (Fig. S1, **5a**), the most stable isomer is triangular in geometry with the C_{2v} symmetry, which can be obtained by replacing the central Cu atom by a Ni atom in ground state Cu_6. This structure is analogous to the result of B. Yin [32] and E. Florez [35]. However, Han have reported that the most stable Cu_5Ni cluster prefers three-dimensional structures with the exchange correlation energy contribution described by the PBE parametrization.

Starting from Cu_6Ni, the ground state structures are inclined to a three-dimensional structure. For Cu_6Ni, the Ni atom substituting for the Cu atom of the Cu_7 cluster [38] conforms a spin singlet capped pentagonal pyramid structure of Cu_6Ni (Fig. 1, **6a**), which is the lowest-energy isomer with the C_{5v} symmetry. This structure is analogous to the result of B. Yin [32] and E. Florez [35]. Our PBE results are closest to the earlier results. For Cu_nNi ($n = 7—12$) clusters, spin multiplicities are doublet (Fig. S1, **7a**), singlet (Fig. S, **8a**), doublet (Fig. S1, **9a**), singlet (Fig. S1, **10a**), doublet (Fig. S1, **11a**), and singlet (Fig. 1, **12a**) respectively. The structures for the Cu_nNi ($n = 7—12$) cluster are C_s (Fig. S1, **7a**), C_{2v} (Fig. S1, **8a**), C_s (Fig. S1, **9a**), C_{2v} (Fig. S1, **10a**), C_1 (Fig. S1, **11a**), and C_1 (Fig. 1, **12a**) respectively. For the Cu_8Ni cluster, the structure is analogous to the result of B. Yin [32] and Han [36]. Just as the Cu_6Ni cluster, Cu_nNi ($n = 7—2$) clusters are also the three-dimensional structures.

In general, the Cu_3Ni, Cu_4Ni and Cu_5Ni clusters adopt the planar structures, and Cu_nNi ($n = 6$, 7, 8, 9, 10, 11, and 12) clusters are more stable as three-dimensional structures rather than planar. The ground state structures found for the Cu_nNi ($n = 3$, 4, 5, 6, 8, and 11) clusters at different levels of computations are usually in good concordance [18—1].

Mechanism of the CO-PROX reaction. Although there is a number of prior experimental studies corroborating the effect of CO coverage on various reactions, to our best knowledge, theoretical studies of the exact mechanism are few. K. Liu *et al.* [4] has summarized two different reaction pathways of PROX: (*a*) Langmuir—Hinshelwood (LH) mechanism which involves the reaction of O_2, H_2 and CO over the platinum group metal catalysts, (*b*) Mar-van Krevlen mechanism (also called the redox mechanism) in which the surface lattice oxygen directly participates in the CO oxidation reaction over the crystal with oxygen and platinum group metal doping. Inspired by the mechanism of PROX catalyzed by the platinum group metals, we explored the possibility of CO-PROX on Cu_nNi ($n = 3—12$) alloy clusters according to the LH mechanism, as shown in scheme 1. Many scholars proposed the reaction via carboxyl (HCOO) and hydroxyl (OH) intermediates for CO-PROX [4, 20, 37, 38].

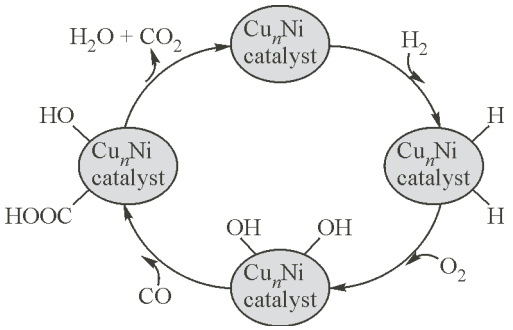

Scheme 1. Langmuir-Hinshelwood catalytic cycle of PROX of CO oxidation in the H_2 stream over the Cu_nNi (3—12) catalysts

However, the formation of COOH is conducted by CO and OH, and hydroxyl is formed via the O and H atoms. Therefore, there are some elementary reaction steps on the Cu_nNi alloy clusters for the PROX reaction of CO

$$H_2 + * \rightarrow 2H*, \quad (1)$$

$$2H* + O_2** \rightarrow OH* + H* + O* + *, \quad (2)$$

$$OH* + H* + O* \rightarrow OH* + OH* + *, \quad (3)$$

$$OH* + OH* + CO* \rightarrow OH* + COOH*, \quad (4)$$

$$OH* + COOH* \rightarrow OCO* + H_2O*, \quad (5)$$

$$OH* + COOH* \rightarrow CO_2* + H_2O*. \quad (6)$$

where * indicates the surface site of clusters.

Adsorption and dissociation of an H_2 molecule on Cu_nNi (n = 3—12) clusters. We study the adsorption and dissociation of an H_2 molecule on Cu_nNi (n = 3—12) clusters by DFT calculations with a PBE correlation functional.

Adsorption and dissociation of an H_2 molecule on Cu_nNi (n = 3—12) clusters. For H_2 adsorption on the optimized Cu_nNi (n = 3—12) clusters with the lowest-energy structures we perform an exhaustive minimum energy structural search. Three types of adsorption sites, i. e. top, edge, and face, have been considered, and the most stable adsorption modes are shown in Fig. 1, ***n*b**. We can see that for the majority of clusters the most favored adsorption site is the Ni top site, which results from the low coordination of Ni atoms placed on the top sites, such as H_2 adsorption on the lowest coordination atoms in SAAS of Cu(111) with a Ni element [39]. It is noted that an H_2 molecule is adsorbed horizontally on the surface of Cu_nNi (n = 4—7, 9, 10, and 12) clusters. For Cu_3Ni, $Cu_{10}Ni$ and $Cu_{11}Ni$, the H_2 molecule slightly shifts to the Cu atom. However, for Cu_8Ni, H_2 is vertically situated on the Ni atom of the cluster. Furthermore, we find that all of the complexes with spin of $2\mu_b$(Cu_3Ni), $3\mu_b$(Cu_4Ni), $2\mu_b$(Cu_5Ni), $2\mu_b$(Cu_7Ni) $1\mu_b$(Cu_8Ni) $2\mu_b$(Cu_9Ni) $1\mu_b$($Cu_{10}Ni$) $2\mu_b$($Cu_{11}Ni$) and $1\mu_b$($Cu_{12}Ni$) have the C_1 symmetry, and $1\mu_b$ (Cu_6Ni) has the C_s symmetry.

The energy and structural properties of the Cu_nNi—H_2 (n = 3—12) complexes shown in Fig. 1, ***n*b** are given in Table 2. For Cu_8Ni—H_2 and $Cu_{11}Ni$—H_2, our results of the adsorption energies about H_2 physisorption on Cu_8Ni and $Cu_{11}Ni$ clusters are –0.01 eV. In addition, the distance between the H_2 molecule and Cu_8Ni, $Cu_{11}Ni$ clusters are 3.08 and 3.07 Å, which is typical physical adsorption. The H—H lengths are no longer than the value of an isolated H_2 molecule (0.75 Å), which all illustrate that their adsorption has the nature of physical adsorption. However, for the Cu_3Ni, Cu_4Ni, Cu_5Ni, Cu_6Ni, Cu_7Ni, Cu_9Ni, $Cu_{10}Ni$, and $Cu_{12}Ni$ clusters, H—H bond distances range from 0.80 to 0.86 Å; the binding energies range from –0.63 to –0.04 eV; and Ni—H bond lengths range from 1.64 to 1.85 Å. We have observed that shorter Ni—H bonds have larger binding energies, which is due to the fact that there are some van der Walls interactions between H_2 and Cu_nNi clusters. The trend of H_2 on Pd_n is similar to that in [40].

Table 2

Spin Multiplicity (M), *Bond Distances* (*d*) *of* H—H, Ni—H *in* Å, *Binding Energy* (BE) *of* $Cu_nNi—H_2$ (n = 3—12). *Activation Energy* (E_a) *in* eV *and Imaginary frequency* (w) *in* cm^{-1} *of* TS

Complexes	M	$d_{H—H}$	$d_{Ni—H}$	BE	E_a	w
$Cu_3Ni—H_2$	2	0.84	1.68	–0.52	0.12	–594.17
$Cu_4Ni—H_2$	3	0.80	1.85	–0.10	0.67	–894.28
$Cu_5Ni—H_2$	2	0.82	1.74	–0.18	0.13	–861.13
$Cu_6Ni—H_2$	1	0.85	1.64	–0.80	0.24	–181.06
$Cu_7Ni—H_2$	2	0.81	1.74	–0.04	0.37	–719.65
$Cu_8Ni—H_2$	1	0.75	3.08	–0.01	0.76	–622.62
$Cu_9Ni—H_2$	2	0.83	1.71	–0.37	0.32	–825.42
$Cu_{10}Ni—H_2$	1	0.83	1.68	–0.37	0.28	–559.64
$Cu_{11}Ni—H_2$	2	0.75	3.07	–0.01	0.22	–862.86
$Cu_{12}Ni—H_2$	1	0.86	1.65	–0.63	0.06	–891.87

The dissociation of an H_2 molecule on Cu_nNi (n = 3—12) clusters is also investigated. Fig. 1, ***n*d** displays the optimized structures of the lowest energy isomers of H_2 dissociation on Cu_nNi (n = 3—12) clusters. From Fig. 1 (***n*d**, n = 3—12) we found that the most stable Cu_nNiH_2 (n = 3—12) complexes always came from those of the lowest-energy bare Cu_nNi (n = 3—12) cluster plus the attached H atoms. The dissociation of an H_2 molecule on Cu_nNi (n = 3—12) clusters are divided into two categories: one is two H atoms sitting on the top of the Ni atom found for Cu_nNi (n = 3, 5, 6, 7, 9, 10, 11, and 12), the other is that two H atoms adsorb on Cu and Ni atoms respectively. For Cu_4Ni (Fig. 1, **4d**) and Cu_8Ni (Fig. 1, **8d**), one H atom is located at the bridge site between the Cu and Ni atoms and another H atom is on the side of the Cu atom.

H_2 dissociation mechanism on Cu_nNi (n = 3—12) clusters. To examine the H_2 dissociative process on Cu_nNi (n = 3—12) clusters, we define the Cu_nNi (n = 3—12) clusters with adsorbed and dissociated H_2 molecules as the reactant and the product respectively. The transition state files related to the H_2 molecule dissociation on Cu_nNi (n = 6, 12) clusters are also displayed in Fig. 1, ***n*b**—***n*d** to clearly understand the reaction process. Other transition state files corresponding to H_2 molecule dissociation on Cu_nNi (n = 3, 4, 5, 7, 8, 9, 10, and 11) are shown in Fig. S1. We have also calculated potential energy surfaces (PESs) for the dissociative chemisorption reactions $H_2 + Cu_nNi \rightarrow Cu_nNiH_2$ (n = 3—12) in Fig. 2. The H_2 dissociation mechanism at the top sites has been studied and interme-

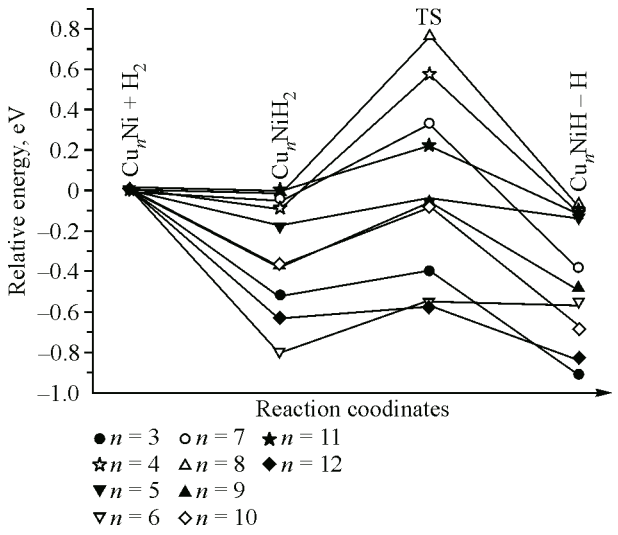

Fig. 2. Dissociation reaction pathway and energetic barriers of H_2 on the Cu_nNi (n = 3—12) clusters

diates (IMs) and transition states (TSs) have been searched. The geometry of transition states and intermediates and energy barriers are given in Fig. 2 to clearly understand the reaction processes. The reaction energy (ΔE_0, including the zero-point energy correction (eV)), activation barrier (eV), imaginary frequency of the transition state $w(cm^{-1})$ are listed in Table 2. The reaction energy (ΔE_0) is directly calculated by the total energy difference between the reactant and the product (negative ΔE_0 means exothermic, whereas positive ΔE_0 means endothermic). The activation barrier is calculated by the total energy difference between the reactant and TS.

The representative PESs of Cu_4Ni, Cu_6Ni, and $Cu_{12}Ni$ are indicated in Fig. 2. Stable adsorption configurations of Fig. 1, **4b**, **6b**, and **12b** are chosen as the initial reactants for the TS search. These structures are energetically favored by 0.52, 0.79, and 0.63 as compared to those of the free H_2 and Cu_nNi reactants (n = 4, 6, and 12) respectively. In the $Cu_nNi—H_2$ complex (n = 4, 6, 12), the H—H bond lengths are 0.80, 0.85, and 0.86 Å, they being only 0.05, 0.10, and 0.11 Å longer than the H—H bond length of the isolated H_2 molecule (0.75 Å). The H_2 dissociation path of Cu_4Ni, Cu_6Ni, and $Cu_{12}Ni$ from $Cu_nNi—H_2$ to Cu_nNiH_2 undergo TS overcoming the energy barrier of 0.67, 0.24, and 0.06 eV respectively. In TS, the H—H bond is split into H—H bond lengths of 1.33, 1.73, and 1.31 Å. TS has only one imaginary frequency that is –894.28, 181.06, and 891.87 cm^{-1} respectively.

In summary, H_2 dissociation on the Cu_nNi (n = 3, 7, 8, 9, 10, 11 and 12) clusters is exothermic as identified by the negative reaction energies (ΔE_0 = –0.06 to –0.39 eV), and on Cu_nNi (n = 4, 5, 6) it is endothermic (ΔE_0 = 0.05 and 0.24 eV). It is found that the calculated energies of Cu_3Ni, Cu_5Ni, Cu_6Ni, Cu_9Ni, and $Cu_{12}Ni$ reaction IMs and TSs along the aforementioned pathways are all below those of reactants, suggesting that these reactions can take place easily. However, for Cu_4Ni, Cu_7Ni, Cu_8Ni, and $Cu_{11}Ni$ do not meet the above rule. The calculated results show that the order of the activation barrier for H_2 dissociation on Cu_nNi (n = 3—12) surfaces is $Cu_{12}Ni < Cu_3Ni < Cu_5Ni < Cu_{11}Ni < Cu_6Ni < Cu_{10}Ni < Cu_9Ni < Cu_7Ni < Cu_4Ni < Cu_8Ni$. The $Cu_{12}Ni$ cluster can bind with the H_2 molecule more strongly (Fig. 1 and Table 2), thereby leading to a higher degree of activation of the H_2 molecule, which tends to yield lower reaction barriers for H_2 dissociation. Thus, $Cu_{12}Ni$ exhibits a larger catalytic activity for H_2 dissociation by the H_2 molecule.

Analysis of the electronic state in the H_2 dissociation reaction on the $Cu_{12}Ni$ cluster. The electronic structure and the charge density difference analysis are carried out to understand how the Ni atom contributes to H_2 adsorption and dissociation. The local density of states (LDOS) projected onto H—H for H_2 molecule dissociation on the $Cu_{12}Ni$ cluster are depicted in Fig. 3. Fig. 3, *a* shows LDOS of isolated H_2 and the $Cu_{12}Ni$ cluster; Fig. 3, *b*—*c* corresponds to LDOS of adsorption, TS, and H_2 molecule dissociation on $Cu_{12}Ni$ clusters respectively. For the H_2 molecule on the $Cu_{12}Ni$ cluster (Fig. 3, *b*) there is an overlap in a range from –7.0 to –4.0 eV between the *s* orbital of H_2 and the Ni *d* state in adsorption of the H_2 molecule on $Cu_{12}Ni$ clusters, indicating a strong interaction between the adsorbed H_2 molecule and the Ni atom. As the reaction proceeds, it can be seen that, from H_2 molecule adsorption on $Cu_{12}Ni$ clusters to TS, orbitals clearly show stronger hybridization between the *s* orbital of the H_2 molecule and the *d* orbital of the Ni atom (–7.0 to –2.0 eV). As shown in Fig. 3, *d* (dissociation of the H_2 molecule on the $Cu_{12}Ni$ cluster), the H_2 *s* orbital is elevated to interact with the Ni *d* orbital at –4.0 eV, which is located above the Fermi level. As these interactions proceed (from Fig. 3, *b*—*c*), we can see that there are no migrations in the *d* orbital of the Cu atom.

O_2 adsorption on Cu_nNiH_2 (n = 3—12) complexes. The O_2 molecule bindings during catalysis are considered as a necessary step for sequent CO-PROX. At first, we study the O_2 molecule behavior during its adsorption on Cu_nNiH_2 (n = 3—12) complexes. Various possible binding sites of the O_2 molecule on the complexes and different relative orientations between the complex and the O_2 molecule have been taken into account for initially designed geometries. After the molecules were optimized, we attached the molecules on the complexes to build the initial geometries of the cluster—molecule complexes.

Fig. 4 displays the optimized structures of the lowest energy isomers of Cu_nNiH_2 (n = 3—12) corresponding to molecular adsorption ($Cu_nNiH_2O_2$). Table 3 presents more details of the geometries, binding energies as well as the electronic properties of the adsorbates. Fig. 4 shows that for Cu_4NiH_2

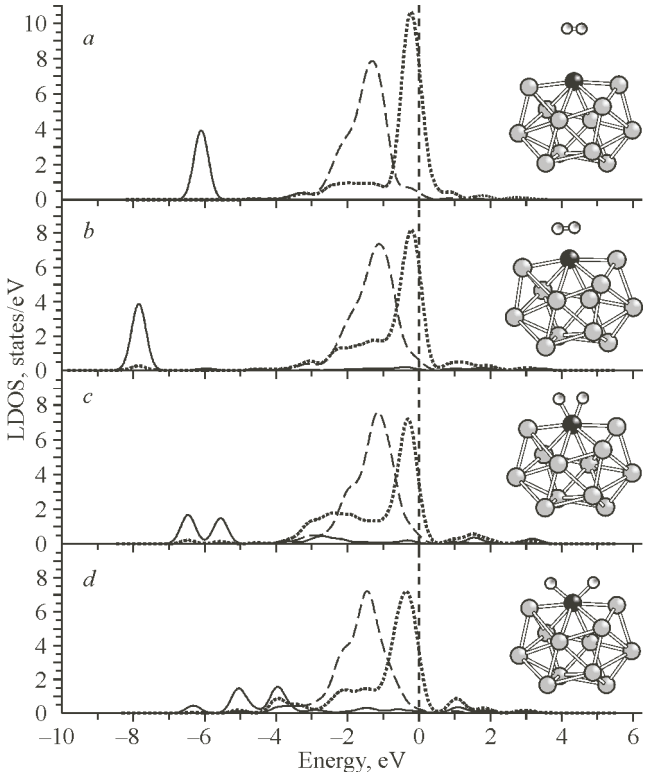

Fig. 3. LDOS projected onto H—H for H_2 molecule dissociation on $Cu_{12}Ni$ clusters. Before interaction (*a*), H_2 molecule adsorption on $Cu_{12}Ni$ clusters (*b*), TS (*c*), dissociation (*d*). Black, dashed, and dotted lines represent LDOS of hydrogen (*s* band), Cu (*d* band), and Ni (*d* band) respectively. The vertical dashed line represents the Fermi level

O_2 adsorption takes place in a top position of the Cu atom with multiplicity M = 3, and for Cu_3NiH_2 and Cu_5NiH_2 O_2 adsorption is located at the bridge site between Cu and Ni atoms with multiplicities M = 3 and 2. While one O atom is located at the bridge site between two Cu atoms, another O atom is on the side of the Ni atom of Cu_nNiH_2 (n = 6, 7, 8, and 9) complexes with spin multiplicities M = 1, 2, 1, and 2 respectively. All of the lowest energy $Cu_nNiH_2O_2$ (n = 3—12) complexes have the C_1 symmetry. Moreover, the O—O bonds have stretched from 1.23 Å in isolation to 1.39 Å ($Cu_3NiH_2O_2$), 1.29 Å ($Cu_4NiH_2O_2$), 1.38 Å ($Cu_5NiH_2O_2$), 1.48 Å ($Cu_6NiH_2O_2$), 1.43 Å ($Cu_7NiH_2O_2$), 1.57 Å ($Cu_8NiH_2O_2$),

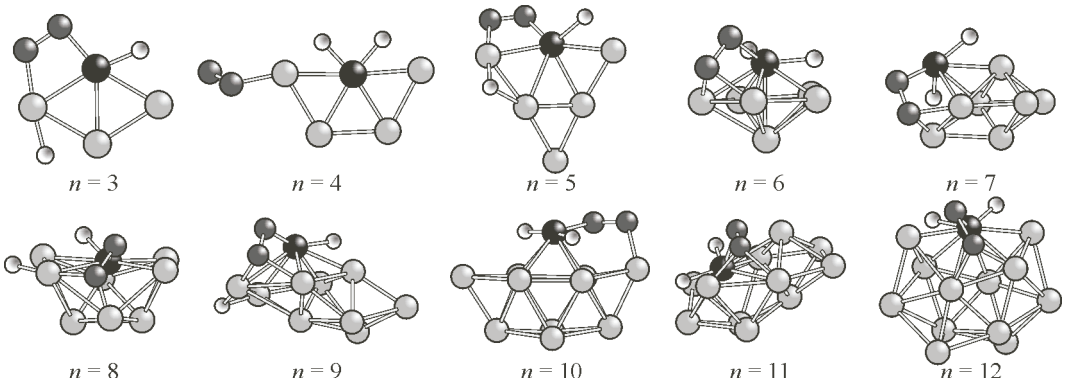

Fig. 4. Optimized geometries of Cu_nNiH_2 (n = 3—12) with an adsorbed O_2 molecule.
Dark grey, black, white, and light grey balls are used for Cu, Ni, H, and O respectively

Table 3

Spin Multiplicity (M), *Point Group* (PG), *adsorption energies* (E_{ad}) *of* O_2 *with* Cu_nNiH_2 (n = 3—12) *in* eV, *Bond Distances* (D) *of the Adsorbates in* Å *and* NBO *Charges of the Adsorbates for* $Cu_nNiH_2O_2$ (n = 3—12) *complexes represented in* Fig. 2

Complexes	M	PG	E_{ad}	$D_{O—O}$	Q_{O2}	Complexes	M	PG	E_{ad}	$D_{O—O}$	Q_{O2}
$Cu_3NiH_2O_2$	2	C_1	–1.80	1.39	–0.70	$Cu_8NiH_2O_2$	1	C_1	–1.40	1.57	–1.25
$Cu_4NiH_2O_2$	3	C_1	–2.02	1.29	–0.33	$Cu_9NiH_2O_2$	2	C_1	–1.95	1.49	–1.03
$Cu_5NiH_2O_2$	2	C_1	–1.85	1.38	–0.71	$Cu_{10}NiH_2O_2$	3	C_1	–1.11	1.37	–0.74
$Cu_6NiH_2O_2$	1	C_1	–0.81	1.48	–1.03	$Cu_{11}NiH_2O_2$	2	C_1	–1.35	1.53	–1.24
$Cu_7NiH_2O_2$	2	C_1	–1.45	1.43	–0.90	$Cu_{12}NiH_2O_2$	1	C_1	–1.00	1.46	–1.06

1.49 Å ($Cu_9NiH_2O_2$), 1.37 Å ($Cu_{10}NiH_2O_2$), 1.53 Å ($Cu_{11}NiH_2O_2$), 1.46 Å ($Cu_{12}NiH_2O_2$) respectively. It is found that the ranking of the O—O bond distance is: $D(Cu_4NiH_2O_2) < D(Cu_{10}NiH_2O_2) < D(Cu_5NiH_2O_2) < D(Cu_3NiH_2O_2) < D(Cu_7NiH_2O_2) < D(Cu_{12}NiH_2O_2) < D(Cu_6NiH_2O_2) < D(Cu_9NiH_2O_2) < D(Cu_{11}NiH_2O_2) < D(Cu_8NiH_2O_2)$. The $^3O_2$ binding energies to Cu_nNiH_2 (n = 3—12) are –1.80, –2.02, –1.85, –0.81, –1.45, –1.40, –1.95, –1.11, –1.35, and 1.00 eV respectively. We found the following interesting trend for trimers: $BE(Cu_4NiH_2O_2) < BE(Cu_9NiH_2O_2) < BE(Cu_5NiH_2O_2) < BE(Cu_3NiH_2O_2) < BE(Cu_7NiH_2O_2) < BE(Cu_8NiH_2O_2) < BE(Cu_{11}NiH_2O_2) < BE(Cu_{10}NiH_2O_2) < BE(Cu_{12}NiH_2O_2) < BE(Cu_6NiH_2O_2)$. For $Cu_nNiH_2O_2$ complexes (n = 3—12), from Table 3 we can see that the NBO charges on O_2 are –0.702, –0.331, –0.71, –1.03, –0.90, –1.25, –1.03, –0.74, –1.24, and –1.06 respectively. We have observed that the O—O bond distance is longer for adsorbed O_2 than that in the free molecule (1.23 Å), being maximum for O_2 adsorption on the Cu_8NiH_2 complex. The NBO charge analysis shows that charge transfer from $Cu_nNiH_2O_2$ (n = 3—12) to adsorbed O_2 takes place in the order: $Q(Cu_4NiH_2O_2) < Q(Cu_3NiH_2O_2) < Q(Cu_5NiH_2O_2) < Q(Cu_{10}NiH_2O_2) < Q(Cu_7NiH_2O_2) < Q(Cu_6NiH_2O_2) < Q(Cu_9NiH_2O_2) < Q(Cu_{12}NiH_2O_2) < Q(Cu_{11}NiH_2O_2) < Q(Cu_8NiH_2O_2)$. For $Cu_4NiH_2O_2$, $Cu_5NiH_2O_2$, $Cu_7NiH_2O_2$, $Cu_6NiH_2O_2$, $Cu_9NiH_2O_2$, $Cu_{11}NiH_2O_2$, and $Cu_8NiH_2O_2$ the trend of the O—O bond distance and the NBO charge is similar, which is due to the fact that metal to oxygen back-donation increases the population of the π* orbital leading to a weakening of O—O bonds, and thereby this bond becomes lengthened.

For $Cu_nNiH_2O_2$ (n = 3, 10, and 12), O—O bond distances have no simple correlation with NBO charges. This is attributed to the complicated mechanism of O_2 binding with Cu_nNiH_2 (n = 3, 10, and 12) complexes. A clear relation is visible between the O_2 binding energy and the NBO charge, which is also due to the fact that metal to oxygen back-donation increases the population of the π* orbital leading to a weakening of the O_2 binding energy.

CO-PROX catalyzed by Cu_nNi (n = 3—12). The LH reaction mechanism has been considered in the present work. This is, $Cu_nNiH_2 + O_{2(gas)} + CO_{(gas)} \rightarrow Cu_nNiH_2 + O_{2(ads)} + CO_{(gas)} \rightarrow Cu_nNiH—OH—O + CO_{(gas)} \rightarrow Cu_nNi(OH)_2 + CO_{(gas)} \rightarrow Cu_nNi(OH)_2 + CO_{(ads)} \rightarrow Cu_nNi—OH—COOH \rightarrow Cu_nNi—OHO—OCO \rightarrow Cu_nNi + H_2O_{(gas)} + CO_{2(gas)}$. Fig. 5 shows the energy profiles for CO-PROX on the ground state surfaces, where Cu_6Ni and $Cu_{12}Ni$ with the geometries of minima and TSs along each path are given to clearly understand the reaction processes. Other energy profiles are displayed in Fig. S2.

Our calculation indicates that the first reaction barrier of Cu_4Ni and Cu_8Ni, the second reaction barrier of Cu_6Ni, Cu_9Ni, and $Cu_{11}Ni$, the third reaction barrier of Cu_5Ni, Cu_7Ni, and $Cu_{12}Ni$, the fourth reaction barrier of Cu_3Ni, and $Cu_{10}Ni$, respectively, are notably higher than those of the neighboring steps. Thus, IM1 to IM2, IM2 to IM3, IM4 to IM5, and IM5 to IM6 are the rate-determining step for Cu_nNi (n = 4 and 8), Cu_nNi (n = 6, 9, and 10), Cu_nNi (n = 5, 7, and 12), and Cu_nNi (n = 1 and 10) respectively.

Here, we select Cu_4Ni and Cu_6Ni as representative model complexes for the planar configuration and the 3D structures on CO-PROX.

CO-PROX catalyzed by Cu_4Ni. As shown in Fig. S1, the CO-PROX mechanism starts from H_2+O_2 co-adsorption forming the structure of IM1, with an adsorption energy of –1.92 eV. Then, ad-

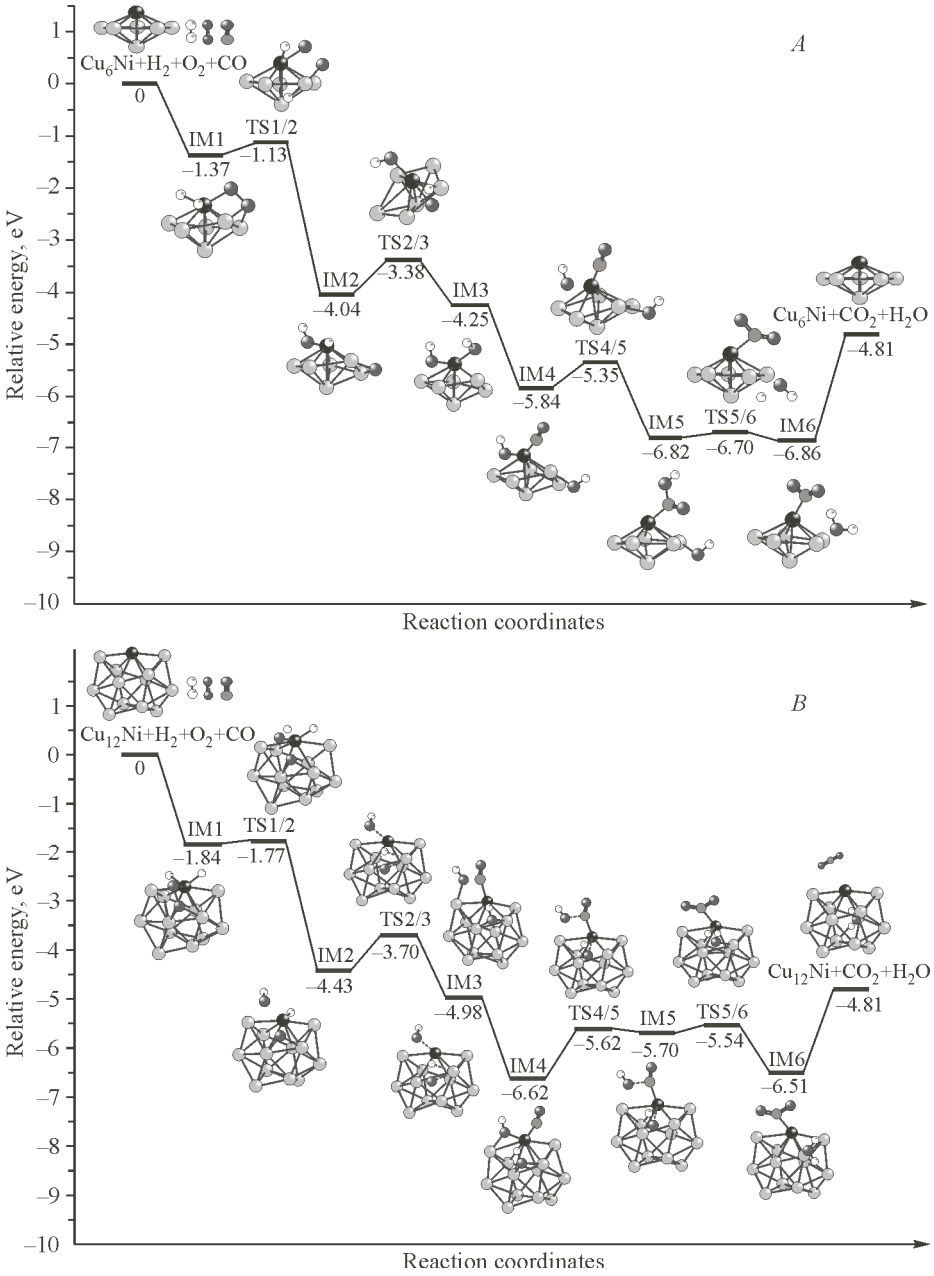

Fig. 5. PESs for the CO-PROX reaction promoted by Cu_6Ni and $Cu_{12}Ni$, eV

sorbed O_2 can approach and bind through its oxygen atom to adsorbed H_2 via TS1/2 (E_a = 0.91 eV, E_a is the activation barrier), forming a stable structure of hydroxyl adsorbate (IM2). This process is found to be the rate-determining step. Subsequently, the second hydroxyl (OH) is formed by another O atom approaching another H atom, which forms the stable complex of IM3 by overcoming the energy barrier of TS2/3 (E_a = 0.71 eV) with an imaginary frequency of –1181.31 cm^{-1}. In the next path, CO tends to be adsorbed on the Ni atom with an adsorption energy of –6.10 eV, forming carboxyl (COOH) complex IM5. The reaction involves TS4/5 (E_a = 0.19 eV). However, this process can be neglected due to a small barrier. In co-adsorption, COOH and OH can react via TS6/7 with a barrier height of 0.78 eV, forming a very stable OCO and OHO adsorbate (IM6). Finally, IM6 can disaggregate into Cu_4Ni, H_2O, and CO_2, indicating the accomplishment of the reaction. As a result, the over-reaction is calculated to be exothermic by 4.81 eV. From this path, because of forming a stable coadsorption

structure IM1, the energy gain in the next hydroxyl formation is larger by 0.91 eV, implying that it is difficult for the structure of hydroxyl to form because of a far distance between the H and O atoms.

To compare the reactivity of Cu_4Ni clusters, we also consider the planar configuration of Cu_3Ni and Cu_5Ni for CO-PROX along the pathway shown in Fig. S1. We can know that the energy barriers for CO-PROX prompted by Cu_3Ni and Cu_5Ni clusters are 1.01 and 1.08 eV respectively, indicating that the Cu_4Ni catalyst is more efficient for CO oxidation than Cu_3Ni and Cu_5Ni catalysts for the planar configuration.

CO-PROX catalyzed by Cu_6Ni cluster. Fig. 5, *A* shows the calculated PES profiles with the optimized geometries of the stationary points. Along the path, first, an O_2 molecule chemisorbs on the Cu_6NiH_2 complex. After co-adsorption, one atomic oxygen starts to approach the adjacent H atom by crossing the energy barrier of 0.24 eV, forming an adsorbed hydroxyl (OH) complex IM2, indicating that the O_2 molecule can readily react with atomic H. IM2 further evolves into IM3, which lies below the entrance by 4.04 eV. The saddle point connecting IM2 and IM3 is TS2/3 with an imaginary frequency of 809.03 cm^{-1}. The barrier to be surmounted from IM2 to TS2/3 is 0.66 eV. This step is the rate-determining step. IM3 then absorbs CO to produce IM4 complex. IM4 can react with IM5 via TS5/6 (E_a = 0.49 eV), forming very stable OCO and OH adsorbates (exothermic by 0.98 eV). Finally, complex IM6 can disaggregate into Cu_6Ni, H_2O, and CO_2, indicating the accomplishment of the reaction, which requires an energy of only 0.16 eV. The overall reaction is calculated to be exothermic by 4.81 eV.

Similarly to the reaction of Cu_6Ni clusters, we designed the pathways for Cu_nNi (n = 7, 8, 9, 10, 11, and 12) in Fig. S2 and Fig. 5 respectively. We find that the activation barriers for CO-PROX prompted by Cu_7Ni, Cu_8Ni, Cu_9Ni, $Cu_{10}Ni$, $Cu_{11}Ni$, and $Cu_{12}Ni$ clusters are 1.05, 0.89, 0.95, 1.11, 1.03, and 1.00 eV.

More specifically, from Fig. S1 it is found that the calculated energies of all reaction IMs and TSs along the aforementioned pathways are all below those of reactants, suggesting that these reactions can take place easily. It looks as if the relative activation barrier of the CO-PROX reactivity on these Cu_nNi (n = 3—12) clusters follows the trend: $E_a(Cu_6Ni) < E_a(Cu_8Ni) < E_a(Cu_4Ni) < E_a(Cu_9Ni) < < E_a(Cu_{12}Ni) < E_a(Cu_3Ni) < E_a(Cu_{11}Ni) < E_a(Cu_7Ni) < E_a(Cu_5Ni) < E_a(Cu_{10}Ni)$. This fact implies that the Cu_6Ni catalyst is more efficient for CO-PROX than the other Cu_nNi (n = 3, 4, 5, 7, 8, 9, 10, 11, and 12) catalysts.

Analysis of the electronic state during PROX of the CO reaction in the H_2 stream on the Cu_6Ni cluster. LDOS of the system projected on the orbitals for the two H atoms, O_2, CO, and OH species, as well as the *d* projected electron density of the bound Cu and Ni atoms, are depicted in Fig. 6. In Fig. 6, a_1—a_5, b_1—b_5 correspond to LDOS of IM1, TS1/2, IM2, TS2/3, IM3 and c_1—c_5, d_1—d_5 show LDOS of IM4, TS4/5, IM5, TS5/6, IM6 respectively. For the two H atoms adsorbed on the Cu *d* state (Fig. 6, a_1), there is an overlap between σ* and the *d* state of Cu and Ni atoms in IM1, indicating a strong interaction between H atoms and Cu and Ni atoms. As seen in Fig. 6, b_1, for the O_2 adsorbate on Cu_6NiH—H, there is an overlap between the 1π orbital of O_2 and the *d* states of Cu and Ni atoms in IM1, indicating strong hybridization between adsorbed O_2 and Cu and Ni atoms. Nevertheless, there is also an overlap between the O_2 2π* orbital and the *d* states of Cu and Ni atoms. The results imply that a positively charge of Cu and Ni atoms rises from more electronegative O. As the reaction proceeds (from Fig. 6 TS1/2 to IM2) the 2π* antibonding orbital of O_2 species spreads back and overlaps with the *d* states of Cu and Ni atoms. However, there is minor overlap between σ* of H atoms and the *d* state of the Cu atom, indicating the formation of hydroxyl. From Fig. 6 TS2/3 to IM4, the 1π orbital of O_2 species spreads back and overlaps with the *d* states of Cu and Ni atoms, but in Fig. 6, a_5 there is no overlap between the σ* and σ orbitals of two H atoms and the *d* states of the Ni and Cu atoms. This implies that two hydroxyl adsorbates are formed. Therefore, the formation of two hydroxyl adsorbates results in LDOS redistribution and the orbitals shift for both H_2 and O_2 species.

As seen in Fig. 6, c_1, there is an overlap between 3σ of the CO molecule and the Ni *d* state in the range from –5 to 0 eV, indicating a strong interaction between the CO molecule and the Ni atom. As seen in Fig. 6, d_1, there are some overlap between 3σ, 4σ, 1π, 2π of OH and the *d* states of Ni and Cu

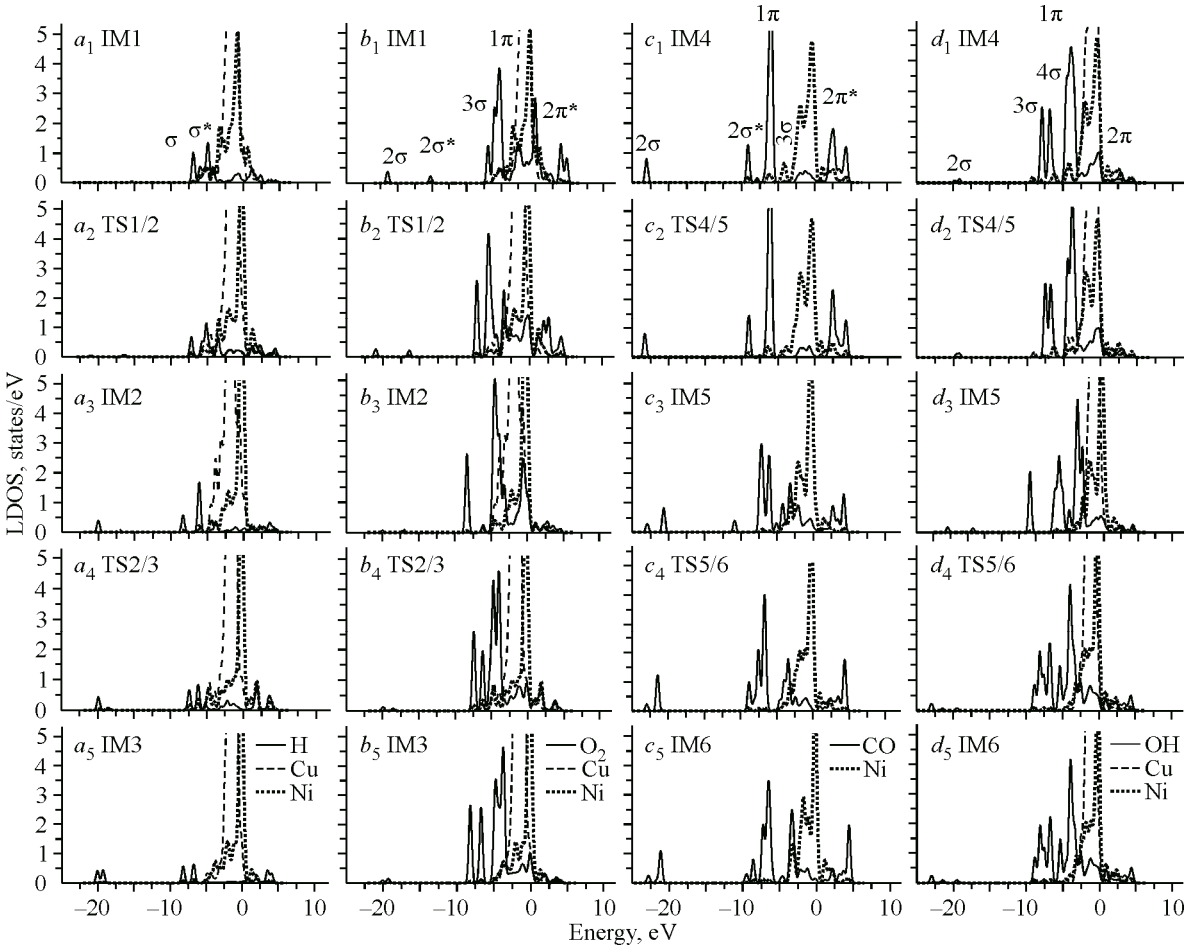

Fig. 6. Calculated LDOS of the system projected on the orbitals for the adsorbed constructs of two H atoms, O_2, CO, and OH species, as well as the *d* projected of the bound Cu and Ni atoms

atoms, indicating a stronger interaction between OH and Ni and Cu atoms. As the reaction proceeds (from Fig. 6 TS5/6 to IM6), the 1π, 3σ states of CO species spread back and overlap with the Ni *d* state, and 4σ,1π states of the OH species overlap with the *d* states of Cu and Ni atoms below 0 eV. For IM5, the formation of the OCOH adsorbate results in the LDOS redistribution, and orbitals shift for both CO and OH species. Due to the scission of the O—H bond of COOH and the formation of C—O and H—OH bonds, a further interaction between COOH and OH species is distinctly observed, as shown in TS6/7 and IM7 of Fig. 6. Finally, in IM7 of Fig. 6, LDOS for the reaction products is similar to LDOS of the separated CO_2 gas phase and H_2O adsorbates on Cu_6Ni, indicating that the CO_2 and H_2O molecules are only physisorbed on the Cu_6Ni clusters.

CONCLUSIONS

In summary, in this work the catalytic properties of Cu_nNi (n = 3—12) clusters in CO-PROX are studied via a thorough DFT sampling of PESs of the cluster systems. The following general conclusions can be drawn from this analysis.

First, even such a simple reaction as CO-PROX, led by a strong thermodynamic driving force and involving a limited number of chemical species, can occur through a series of elementary reactions, ranging from H_2 adsorption and dissociation on Cu_nNi (n = 3—12) clusters; O_2 combined two H atoms, forming two hydroxyl adsorbates, specifically, one of the hydroxyl adsorbates and a successive CO reaction with carboxyl and the hydroxyl and carboxyl reaction with carbon dioxide and water.

Second, the ground state structures found for the Cu_nNi (n = 3, 4, 5, 6, 8, and 11) clusters from different levels of computations are usually in good concordance [18—21]. Moreover, the growth pattern for Cu_nNi (n = 3—6, 8—12) clusters is the Ni atom occupying the central position of Cu_nNi clusters. However, in the structures of Cu_7Ni the Ni atom occupies a peripheral position.

Third, H_2 dissociation on the Cu_nNi (n = 3, 7, 8, 9, 10, 11, and 12) clusters is exothermic as identified by the negative reaction energies (ΔE_0 = –0.06 to –0.39 eV), and on Cu_nNi (n = 4, 5, 6) it is endothermic (ΔE_0 = 0.05 and 0.24 eV). It is found that the calculated energies of Cu_3Ni, Cu_5Ni, Cu_6Ni, Cu_9Ni, and $Cu_{12}Ni$ reaction IMs and TSs along the aforementioned pathways are all below those of reactants, suggesting that these reactions can take place easily. However, for Cu_4Ni, Cu_7Ni, Cu_8Ni, and $Cu_{11}Ni$ do not meet the above rule. Moreover, the calculated results show that the order of the activation barrier for H_2 dissociation on Cu_nNi (n = 3—12) surfaces is $Cu_{12}Ni < Cu_3Ni < Cu_5Ni < Cu_{11}Ni < Cu_6Ni < Cu_{10}Ni < Cu_9Ni < Cu_7Ni < Cu_4Ni < Cu_8Ni$. $Cu_{12}Ni$ clusters can bind more strongly with the H_2 molecule (Fig. 1 and Table 2), thereby leading to a higher degree of activation of the H_2 molecule, which tends to yield lower reaction barriers for H_2 dissociation. Thus, $Cu_{12}Ni$ exhibits a larger catalytic activity for H_2 dissociation.

Finally, in the present case, the calculated energies of all reaction IMs and TSs along the aforementioned pathways are all below those of reactants, suggesting that these reactions can take place easily. The relative activation barrier of the CO-PROX reactivity on these Cu_nNi (n = 3—12) clusters follows the trend: $E_a(Cu_6Ni) < E_a(Cu_8Ni) < E_a(Cu_4Ni) < E_a(Cu_9Ni) < E_a(Cu_{12}Ni) < E_a(Cu_3Ni) < E_a(Cu_{11}Ni) < E_a(Cu_7Ni) < E_a(Cu_5Ni) < E_a(Cu_{10}Ni)$. This fact implies that the Cu_6Ni catalyst is more efficient for CO-PROX than the other Cu_nNi (n = 3, 4, 5, 7, 8, 9, 10, 11, and 12) catalysts.

We believe that the present analysis offers interesting perspectives in the understanding and exploitation of heterogeneous subnanocatalysts, while pointing to the need of efficient algorithms for the structural exploration and sampling to achieve predictive computational science.

This work was financially supported by the National Natural Science Foundation of China (Grant No. 20603021), the Natural Science Foundation of Shanxi (Grant No. 2013011009-6), the High School 131 Leading Talent Project of Shanxi, Undergraduate Training Programs for Innovation and Entrepreneurship of Shanxi Province (Grant No. 105088, 2015537, WL2015CXCY-SJ-01), Shanxi Normal University (WL2015CXCY-YJ-18), Teaching Reform Project of Shanxi Normal University (WL2015JGXM-YJ-13), and Graduate student education innovation project of Shanxi Normal University.

REFERENCES

1. *Carlton C.E., Chen S., Ferreira P.J., Allard L.F., Horn Y.S.* // J. Phys. Chem. Lett. – 2012. – **3**. – P. 161 – 166.
2. *Wakita H., Ukai K., Takeguchi T., Ueda W.* // J. Phys. Chem. C. – 2007. – **111**. – P. 2205 – 2211.
3. *Lauzze K.C., Chmielewski D.J.* // Ind. Eng. Chem. Res. – 2006. – **45**. – P. 4661 – 4670.
4. *Liu K., Wang A., Zhang T.* // ACS Catal. – 2012. – **2**. – P. 1165 – 1178.
5. *Cohn J.G.E.* // Patented Nov. – 1965. – **9**. – P. 3216782.
6. *Gustafson J., Westerstro R., Balmes O., Resta A., Rijn R., Torrelles X., Herbschleb C.T., Frenken J.W.M., Lundgren E.* // J. Phys. Chem. C. – 2010. – **114**. – P. 4580 – 4583.
7. *Tabakova T., Manzoli M., Vindigni F., Idakiev V., Boccuzzi F.* // J. Phys. Chem. A. – 2010. – **114**. – P. 3909 – 3915.
8. *Laguna O.H., Hernandez W.Y., Arzamendi G., Gandia L.M., Centeno M.A., Odriozola J.A.* // Fuel. – 2014. – **118**. – P. 176 – 185.
9. *Sangeetha P., Chang L.H., Chen Y.W.* // Ind. Eng. Chem. Res. – 2009. – **48**. – P. 5666 – 5670.
10. *Fukuoka A., Kimura J., Oshio T., Sakamoto Y., Ichikawa M.* // J. Am. Chem. Soc. – 2007. – **129**. – P. 10120 – 10125.
11. *Zhang H., Jin M., Liu H., Wang J., Kim M.J., Yang D., Xie Z., Liu J., Xia Y.* // AcsNano. – 2011. – **5**. – P. 8212 – 8222.
12. *Ko E.Y., Park E.D., Lee H.C., Lee D., Kim S.* // Angew. Chem. Int. Ed. – 2007. – **46**. – P. 734 – 737.
13. *Pu Z.Y., Liu X.S., Jia A.P., Xie Y.L., Lu J.Q., Luo M.F.* // J. Phys. Chem. C. – 2008. – **112**. – P. 15045 – 15051.

14. *Yang B., Burch R., Hardacre G., Headdock., Hu P.* // ACS Catal. – 2012. – **2**. – P. 1027 – 1032.
15. *Wei W., Dai Y., Huang B.* // J. Phys. Chem. C. – 2011. – **115**. – P. 18597 – 18602.
16. *Umamaheswari V., Hartmann M., Pöppl A.* // J. Phys. Chem. B. – 2005. – **109**. – P. 1537 – 1546.
17. *Shen S., Zhao L., Zhou Z., Guo L.* // J. Phys. Chem. C. – 2008. – **112**. – P. 16148 – 16155.
18. *Arias A.M., Gamarra D., García M.F., Hornés A., Bera P., Koppány Z., Schay Z.* // Catal. Today. – 2009. – **143**. – P. 211 – 217.
19. *Liua X., Wanga A., Zhanga T., Sub D., Mouc C.Y.* // Catal. Today. – 2011. – **160**. – P. 103 – 108.
20. *Komatsu T., Takasaki M., Ozawa K., Furukawa S., Muramatsun A.* // J. Phys. Chem. C. – 2013. – **117**. – P. 10483 – 10491.
21. *Kugai J., Moriya T., Seino S., Nakagawa T., Ohkubo Y., Nitani H., Ueno K., Yamamoto T.A.* // J. Phys. Chem. C. – 2013. – **117**. – P. 5742 – 5751.
22. *Gan L.Y., Tian R.Y., Yang X.B., Lu H.D., Zhao Y.J.* // J. Phys. Chem. C. – 2012. – **116**. – P. 745 – 752.
23. *Frisch M.J., Trucks G.W., Schlegel H.B., Scuseria G.E., Robb M.A., Cheeseman J.R., Scalmani G., Barone V., Mennucci B., Petersson G.A., Nakatsuji H., Caricato M., Li X., Hratchian H.P., Izmaylov A.F., Bloino J., Zheng G., Sonnenberg J.L., Hada M., Ehara M., Toyota K., Fukuda R., Hasegawa J., Ishida M., Nakajima T., Honda Y., Kitao O., Nakai H., Vreven T., Montgomery J.A. Jr., Peralta J.E., Ogliaro F., Bearpark M., Hey J.J., Brothers E., Kudin K.N., Staroverov V.N., Kobayashi R., Normand J., Raghavachari K., Rendell A., Burant J.C., Iyengar S.S., Tomasi J., Cossi M., Rega N., Millam J.M., Klene M., Knox J.E., Cross J.B., Bakken V., Adamo C., Jaramillo J., Gomperts R., Stratmann R.E., Yazyev O., Austin A.J., Cammi R., Pomelli C., Ochterski J.W., Martin R.L., Morokuma K., Zakrzewski V.G., Voth G A., Salvador P., Dannenberg J.J., Dapprich S., Daniels A.D., Farkas O., Foresman J.B., Ortiz J.V., Cioslowski J. Fox D.J.* Gaussian 09, Revision A.1, Gaussian, Inc. Wallingford CT. 2009.
24. *Perdew J.P., Burke K., Ernzerhof M.* // Phys. Rev. Lett. – 1996. – **77**. – P. 3865 – 3868.
25. *Wadt W.R., Hay P.J.* // J. Chem. Phys. – 1985. – **82**. – P. 270 – 283.
26. *Hay P.J., Wadt W.R.* // J. Chem. Phys. – 1985. – **82**. – P. 299 – 310.
27. *Peng C., Ayala P.Y. Schlegel H.B.* // J. Comput. Chem. – 1996. – **17**. – P. 49 – 56.
28. (a) *Gonzalez C., Schlegel H.B.* // J. Chem. Phys. – 1989. – **90**. – P. 2154 – 2161.
29. (b) *Gonzalez C., Schlegel H.B.* // J. Chem. Phys. – 1990. – **54**. – P. 5523 – 5527.
30. *Glendening E.D., Reed A.E., Carpenter J.E., Weinhold.* NBO. – Theoretical Chemistry Institute, University of Wisconsin Madison, 2001.
31. *Huber K.P., Herzberg G.* Constants of Diatomic Molecules. – Van Nostrand Reinhold, New York, 1979.
32. *Morse M.D.* // Chem. Rev. – 1988. – **86**. – P. 1049 – 1109.
33. *Yin B., Yin Y., Lei Y., Dong L., Zhang Y.* // Chem. Phys. Lett. – 2011. – **509**. – P. 192 – 197.
34. *Cao Z., Wang Y., Zhu J., Wu W., Zhang Q.* // J. Phys. Chem. B. – 2002. – **106**. – P. 9649 – 9654.
35. *Yang M., Yang F., Jackson K.A., Jellinek J.* // J. Chem. Phys. – 2010. – **132**. – P. 064306.
36. *Florez E., Mondragón F., Fuentealba P.* // J. Phys. Chem. B. – 2006. – **110**. – P. 13793 – 13798.
37. *Han S.L., Xue X., Nie X.C., Zhai H., Wang F., Sun Q., Jia Y., Li S.F., Guo Z.X.* // Phys. Lett. A. – 2010. – **374**. – P. 4324 – 4330.
38. *Tanaka K.M., Shou Y.* // J. Phys. Chem. C. – 2010. – **114**. – P. 16917 – 16923.
39. *Tanaka K., Shou M., He H., Shi X., Zhang X.* // J. Phys. Chem. C. – 2009. – **113**. – P. 12427 – 12433.
40. *Pelzer A.W., Jellinek J., Jackson K.A.* // J. Phys. Chem. A. – 2013. – **117**. – P. 10407 – 10415.
41. *Fu Q., Luo Y.* // J. Phys. Chem. C. – 2013. – **117**. – P. 14618 – 14624.